Geometrical frustration of an extended Hubbard diamond chain in the quasiatomic limit

Onofre Rojas,[1] S. M. de Souza,[1] and N. S. Ananikian[1,2]
[1]*Departamento de Ciencias Exatas, Universidade Federal de Lavras, CP 3037, 37200-000 Lavras-MG, Brazil*
[2]*A. I. Alikhanyan National Science Laboratory, 0036 Yerevan, Armenia*
(Received 19 January 2012; published 21 June 2012)

We study the geometrical frustration of an extended Hubbard model on a diamond chain, where vertical lines correspond to the hopping and repulsive Coulomb interaction terms between sites while the remaining lines represent only the Coulomb repulsion term. The phase diagrams at zero temperature show quite curious phases: five types of frustrated states and four types of nonfrustrated states, ordered antiferromagnetically. Although a decoration transformation was derived for spin-coupling systems, this approach can be applied to electron-coupling systems. Thus the extended Hubbard model can be mapped onto another effective extended Hubbard model in the atomic limit with additional three- and four-body couplings. This effective model is solved exactly using the transfer-matrix method. In addition, using the exact solution of this model, we discuss several thermodynamic properties away from the half-filled band, such as chemical potential behavior, electronic density, and entropy, for which we study geometrical frustration. Consequently, we investigate the specific heat as well.

DOI: 10.1103/PhysRevE.85.061123 PACS number(s): 05.50.+q, 75.10.Lp, 71.10.Fd, 71.27.+a

I. INTRODUCTION

The Hubbard model is one of the simplest models for strongly interacting electron systems. In general, it is difficult to perform a rigorous analysis of the model, and exact results have only been obtained in particular cases [1]. On the other hand, geometrical frustration in strongly correlated electron systems has attracted a great deal of interest over the past decades [2,3]. Due to the competition between nearest and next-nearest exchange coupling, the inorganic spin-Peierls compound exhibits a transition from a gapless phase to a gapped dimerized ground state [4]. The quantum phase transition point from the gapless phase to the gapped dimerized phase of this model was first determined by Okamoto and Nomura [5].

The interplay between geometrical frustration and strong electron correlation results in a complicated phase diagram containing many interesting phases, including the spin-gapped metallic phase, the disorder magnetic insulation phase, and the Heisenberg insulator [6]. The Hubbard model on the triangular lattice exhibits a transition from a paramagnetic metal to an antiferromagnetic insulator as the Hubbard on-site repulsion gradually grows [7].

In a pioneering theoretical paper [8], Hida predicted the appearance of the magnetization plateau using the numerical diagonalization of a finite-size system. In the framework of the transfer-matrix and dynamical recursive approaches, the frustrated magnetization plateaus were obtained for ferromagnetic-ferromagnetic-antiferromagnetic kagome chains as well as a zigzag ladder with multispin exchanges [9–11]. Magnetization plateaus via the chemical potential or a magnetic field have been studied in the Hubbard model for small nanoclusters using exact numerical diagonalization of the average electron density [12,13].

Recently, geometrical frustration of the Hubbard model was widely studied. In particular, the diamond chain structure was considered by Derzhko *et al*. [14,15], and they discussed the frustration for a special class of lattice. Montenegro-Filho and Coutinho-Filho [16] also considered the doped AB_2 Hubbard chain, both in the weak-coupling and the infinite-U limit (atomic limit). They studied interesting phases as a function of hole doping away from half-filled band. Mancini [17,18] presented the exact solution of an extended one-dimensional Hubbard model in the atomic limit. He obtained the chemical potential plateaus of the particle density, of the on-site potential at zero temperature, and he studied the thermodynamic charge susceptibility, compressibility at finite temperature, as well as other physical quantities. Vidal *et al*. [19] also discussed two interacting particles evolving in a diamond chain structure embedded in a magnetic field. The interaction of the particles leads to the strong localization induced by the magnetic field for the particular value of a flux. An analogous model was also studied by Rossler and Mainemer [20]. The Hubbard model in another quasi-one-dimensional triangular structure was studied by Wang [21]. The latter indicated that for a small hopping term, the system exhibits short-range antiferromagnetic correlation, whereas when the hopping terms become greater than the critical point, there is a transition from an antiferromagnetic state to a frustrated one. Moreover, the insulator-metal transition takes place at a hopping interaction that is even greater than another critical point. In addition, Gulacsi *et al*. [22,23] discussed the diamond Hubbard chain in a magnetic field and a wide range of properties, such as flat-band ferromagnetism and the correlation-induced metallic, half-metallic process. The spinless versions of the Hubbard model on a diamond chain were also recently investigated through exact analytical solution [24], and Lopes and Dias [25] performed a detailed investigation using the exact diagonalization approach.

In the past decade, several diamond chain structures were discussed. Some of them were motivated by real materials such as $Cu_3(CO_3)_2(OH)_2$, known as azurite, which is an interesting quantum antiferromagnetic model described by the Heisenberg model on a generalized diamond chain. Honecker *et al*. [26] studied the dynamic and thermodynamic properties for this model. In addition, Pereira *et al*. [27] investigated the magnetization plateau of delocalized interstitial spins on a diamond chain, and they detected the magnetocaloric effect in a kinetically frustrated diamond chain [28]. Quite recently,

 ©2012 American Physical Society

Lisnii [29] studied a distorted diamond Ising-Hubbard chain, and that model exhibited geometrical frustration also. A further investigation regarding exact evidence for spontaneous antiferromagnetic long-range order in the two-dimensional hybrid model of localized Ising spins and itinerant electrons was discussed by Strečka *et al*. [30,31]. Moreover, the thermodynamics of the Ising-Heisenberg model on a diamondlike chain was widely discussed in Refs. [32–35], and thermal entanglement was considered by Ananikian *et al*. [36].

On the other hand, the analytical exact solution is rather amazing because the exact result is always useful to manipulate the numerical results. Therefore, the exact solutions of the models are of great importance, so our main goal is to obtain an exact solution for the extended Hubbard model on a diamond chain in the quasiatomic limit. Research on the extended Hubbard diamond chain model without the hopping of electrons between the nodal sites is based on three main points.

First of all, the 1/3 magnetization plateau—the double peaks both in the magnetic susceptibility and the specific heat—was observed in the experimental measurements [37,38] according to the experiments of the natural mineral azurite. Theoretical calculations of the one-dimensional Hubbard model, as well as the experimental results of the exchange dimer (interstitial sites) parameter and their descriptions of the various theoretical models, are presented. It should be noted that the dimers (interstitial sites) exchange much more strongly than those nodal sites. Various types of theoretical Heisenberg approximate methods were proposed. The renormalization of the density matrix renormalization group of the transfer matrix, the density functional theory, the high-temperature expansion, and Lanczos diagonalization on a diamond chain are all intended to explain the experimental measurements (magnetization plateau and the double top) in the natural mineral azurite [39]. All of these theoretical studies are approximate. There is another possibility. Since dimer interaction is much higher than the rest, it can be represented as an exactly solvable Ising-Heisenberg model. In addition, experimental data on the magnetization plateau coincide with the approximation of the Ising-Heisenberg model [27,32,36,40] and the extended Hubbard model without the hopping of electrons between the nodal sites [24] on a diamond chain.

The second point is quantum block-block entanglement. This is carried out by the exact diagonalization technique in the one-dimensional extended Hubbard model, and it is calculated for finite size ($L = 10$) [41]. When the absolute value of nearest-neighbor Coulomb interactions (our case) becomes smaller, the effect of the hopping term and the on-site interaction cannot be neglected. Finally, we would like to point out that although the results obtained in this paper are for the two-site (dimer) system, their qualitative features are the same as those of larger systems.

The third point is the experimental observation of the double peaks both in the magnetic susceptibility and the specific heat [27,39,42]. It may be described exactly by the extended Hubbard diamond chain model without the hopping of electrons or holes between the nodal sites. This phenomenon is particularly important in the quantum case.

This paper is organized as follows. In Sec. II, we present the extended Hubbard model on a diamond chain. We discuss the phase diagram at zero temperature in Sec. III. In Sec. IV, we present the exact solution of the model. In Sec. V, we discuss the thermodynamic properties of the model, such as electronic density, internal energy, compressibility, entropy, and specific heat away from the half-filled band. Finally, Sec. VI contains concluding remarks.

II. THE EXTENDED HUBBARD MODEL

In this paper, we will consider the extended Hubbard model on a diamond chain, as represented schematically in Fig. 1. In the present model, we consider the hopping term t between sites a and b. In addition, there is the on-site Coulomb repulsion interaction term denoted by U and the nearest-neighbor repulsion interaction term denoted by V. We assume also that this model has an arbitrary particle density, so we will include a chemical potential term denoted by μ. Therefore, the Hamiltonian of this model can be expressed by

$$\boldsymbol{H} = \sum_{i=1}^{N} \boldsymbol{H}_{i,i+1}, \tag{1}$$

with N being the number of cells (sites a, b, and c), whereas $\boldsymbol{H}_{i,i+1}$ is given by

$$\begin{aligned}\boldsymbol{H}_{i,i+1} &= -t \sum_{\sigma=\downarrow,\uparrow} (\boldsymbol{a}^{\dagger}_{i,\sigma}\boldsymbol{b}_{i,\sigma} + \boldsymbol{a}_{i,\sigma}\boldsymbol{b}^{\dagger}_{i,\sigma}) \\ &\quad - \mu\left[\boldsymbol{n}^{a}_{i} + \boldsymbol{n}^{b}_{i} + \frac{1}{2}\left(\boldsymbol{n}^{c}_{i} + \boldsymbol{n}^{c}_{i+1}\right)\right] \\ &\quad + U\left[\boldsymbol{n}^{a}_{i,\uparrow}\boldsymbol{n}^{a}_{i,\downarrow} + \boldsymbol{n}^{b}_{i,\uparrow}\boldsymbol{n}^{b}_{i,\downarrow} + \frac{1}{2}\left(\boldsymbol{n}^{c}_{i,\uparrow}\boldsymbol{n}^{c}_{i,\downarrow} + \boldsymbol{n}^{c}_{i+1,\uparrow}\boldsymbol{n}^{c}_{i+1,\downarrow}\right)\right] \\ &\quad + V\left[\boldsymbol{n}^{a}_{i}\boldsymbol{n}^{b}_{i} + \frac{1}{2}\left(\boldsymbol{n}^{a}_{i} + \boldsymbol{n}^{b}_{i}\right)\left(\boldsymbol{n}^{c}_{i} + \boldsymbol{n}^{c}_{i+1}\right)\right],\end{aligned} \tag{2}$$

where $\boldsymbol{a}_{i,\sigma}$ and $\boldsymbol{b}_{i,\sigma}$ ($\boldsymbol{a}^{\dagger}_{i,\sigma}$ and $\boldsymbol{b}^{\dagger}_{i,\sigma}$) represent the Fermi annihilation (creation) operator for the Hubbard model, σ denotes the electron spin, and $\boldsymbol{n}^{\alpha}_{i,\sigma}$ indicates the number operator, with $\alpha = \{a,b,c\}$. Using this number operator, we define also the operators $\boldsymbol{n}^{\alpha}_{i} = \boldsymbol{n}^{\alpha}_{i,\uparrow} + \boldsymbol{n}^{\alpha}_{i,\downarrow}$.

In order to write the Hamiltonian (2) in a more compact form, we can define the following operators:

$$\boldsymbol{p}_{i,i+1} = \tfrac{1}{2}\left(\boldsymbol{n}^{c}_{i} + \boldsymbol{n}^{c}_{i+1}\right), \quad \boldsymbol{q}_{i,i+1} = \tfrac{1}{2}\left(\boldsymbol{n}^{c}_{i,\uparrow}\boldsymbol{n}^{c}_{i,\downarrow} + \boldsymbol{n}^{c}_{i+1,\uparrow}\boldsymbol{n}^{c}_{i+1,\downarrow}\right). \tag{3}$$

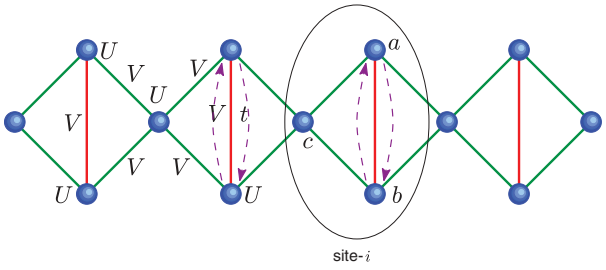

FIG. 1. (Color online) Schematic representation of the extended Hubbard model on a diamond chain.

Using these operators, we can rewrite the Hamiltonian (2) as follows:

$$\begin{aligned}\boldsymbol{H}_{i,i+1} = &-t\sum_{\sigma=\downarrow,\uparrow}(\boldsymbol{a}^{\dagger}_{i,\sigma}\boldsymbol{b}_{i,\sigma}+\boldsymbol{a}_{i,\sigma}\boldsymbol{b}^{\dagger}_{i,\sigma})\\ &-(\mu-V\boldsymbol{p}_{i,i+1})\left(\boldsymbol{n}^{a}_{i}+\boldsymbol{n}^{b}_{i}\right)+U\left(\boldsymbol{n}^{a}_{i,\uparrow}\boldsymbol{n}^{a}_{i,\downarrow}+\boldsymbol{n}^{b}_{i,\uparrow}\boldsymbol{n}^{b}_{i,\downarrow}\right)\\ &+V\boldsymbol{n}^{a}_{i}\boldsymbol{n}^{b}_{i}-\mu\boldsymbol{p}_{i,i+1}+U\boldsymbol{q}_{i,i+1}. \qquad (4)\end{aligned}$$

The particle-hole symmetry can be analyzed in a similar way, as discussed in Ref. [24]. The phase diagram in the half-filled band can be obtained using the following restriction for the chemical potential: $\mu = U/2 + 2V$. This relation could be obtained by using the particle-hole symmetry in a similar way, as discussed in Ref. [24].

III. THE PHASE DIAGRAM

In order to study the phase diagram at zero temperature, first we need to diagonalize the Hamiltonian (4) at sites a and b. We will use $m = \{0,\ldots,4\}$ to denote the total number of mobile electrons per unit cell at sites a and b, while n_c will indicate the number of electrons per unit cell at site c. The Hamiltonian at sites a and b can be written as a 16×16 matrix, but this matrix can be constructed as a block matrix. In the largest block matrix we have 4×4, therefore the eigenvalues and eigenvectors of this matrix are expressed below as follows:

(a) For a state with $m = 0$ particles,

$$\lambda_0 = \boldsymbol{D}_0, \quad |S_0\rangle = |0,0\rangle, \qquad (5)$$

where $\boldsymbol{D}_m = -(\mu - V\boldsymbol{p}_{i,i+1})m - \mu\boldsymbol{p}_{i,i+1} + U\boldsymbol{q}_{i,i+1}$, while the state $|S_0\rangle = |0,0\rangle$ means there are no particles at sites a and b, respectively.

(b) For a state with $m = 1$ particle,

$$\lambda^{(\pm)}_{\sigma} = \boldsymbol{D}_1 \pm t, \quad |S^{(\pm)}_{\sigma}\rangle = \frac{1}{\sqrt{2}}\left(|0,\sigma\rangle \mp |\sigma,0\rangle\right), \qquad (6)$$

where $|S^{(\pm)}_{\sigma}\rangle$ means there is one particle at site a or b with either spin up or down.

(c) For a state with $m = 2$ particles,

$$\lambda_{2\sigma} = \boldsymbol{D}_2 + V, \quad |S_{2\sigma}\rangle = |\sigma,\sigma\rangle, \qquad (7)$$

$$\lambda^{(1)}_{\downarrow\uparrow} = \boldsymbol{D}_2 + U, \quad |S^{(1)}_{\downarrow\uparrow}\rangle = \frac{1}{\sqrt{2}}(|\downarrow\uparrow,0\rangle - |0,\downarrow\uparrow\rangle), \qquad (8)$$

$$\lambda^{(\pm)}_{\downarrow\uparrow} = \boldsymbol{D}_2 + V + \frac{\theta_{\pm}t}{2}, \qquad (9)$$

$$|S^{(\pm)}_{\downarrow\uparrow}\rangle = \frac{1}{\zeta_{\mp}}[|\downarrow\uparrow,0\rangle + |0,\downarrow\uparrow\rangle + \theta_{\mp}(|\uparrow,\downarrow\rangle + |\downarrow,\uparrow\rangle)], \qquad (10)$$

$$\lambda^{(2)}_{\downarrow\uparrow} = \boldsymbol{D}_2 + V, \quad |S^{(2)}_{\downarrow\uparrow}\rangle = \frac{1}{\sqrt{2}}(|\uparrow,\downarrow\rangle - |\downarrow,\uparrow\rangle), \qquad (11)$$

where

$$\zeta_{\pm} = \sqrt{2 + \frac{\theta^2_{\pm}}{8}}, \qquad (12)$$

$$\theta_{\pm} = \frac{U - V \pm \sqrt{(U-V)^2 + 16t^2}}{t}. \qquad (13)$$

TABLE I. The first column (n_t) represents the number of particles per unit cell. The second and third columns show the ground-state energy per unit cell and its corresponding ground state, respectively.

n_t	Ground-state energy	Ground state
0	0	$\lvert\mathsf{S_0}\rangle = \lvert\mathsf{Vac}\rangle = \prod_i \lvert S_0\rangle_i \otimes \lvert 0\rangle_i$
1	$-\mu - t$	$\lvert\mathsf{S_1}\rangle = \lvert\mathsf{FRU_1}\rangle = \prod_i \lvert S^{(-)}_{\sigma}\rangle_i \otimes \lvert 0\rangle_i$
2	$-2\mu + V + \frac{\theta_- t}{2}$	$\lvert\mathsf{S_2}\rangle = \lvert\mathsf{AFM_2}\rangle = \prod_i \lvert S^{(-)}_{\downarrow\uparrow}\rangle_i \otimes \lvert 0\rangle_i$
2	$-2\mu - t + V$	$\lvert\bar{\mathsf{S}}_2\rangle = \lvert\mathsf{FRU_2}\rangle = \prod_i \lvert S^{(-)}_{\sigma}\rangle_i \otimes \lvert 1\rangle_i$
3	$-3\mu + 3V + \frac{\theta_- t}{2}$	$\lvert\mathsf{S_3}\rangle = \lvert\mathsf{FRU_3}\rangle = \prod_i \lvert S^{(-)}_{\downarrow\uparrow}\rangle_i \otimes \lvert 1\rangle_i$
4	$-4\mu + 5V + U + \frac{\theta_- t}{2}$	$\lvert\mathsf{S_4}\rangle = \lvert\mathsf{AFM_4}\rangle = \prod_i \lvert S^{(-)}_{\downarrow\uparrow}\rangle_i \otimes \lvert 2\rangle_i$
4	$-4\mu - t + 5V + U$	$\lvert\bar{\mathsf{S}}_4\rangle = \lvert\mathsf{FRU_4}\rangle = \prod_i \lvert S^{(-)}_{\downarrow\uparrow\sigma}\rangle_i \otimes \lvert 1\rangle_i$
5	$-5\mu + 8V + 2U - t$	$\lvert\mathsf{S_5}\rangle = \lvert\mathsf{FRU_5}\rangle = \prod_i \lvert S^{(-)}_{\downarrow\uparrow\sigma}\rangle_i \otimes \lvert 2\rangle_i$
6	$-6\mu + 12V + 3U$	$\lvert\mathsf{S_6}\rangle = \lvert\mathsf{Full}\rangle = \prod_i \lvert S_{\downarrow\uparrow\downarrow\uparrow}\rangle_i \otimes \lvert 2\rangle_i$

The states $|S_{2\sigma}\rangle$ and $|S^{(\pm)}_{\downarrow\uparrow}\rangle$ are defined in a similar way as in the previous case, with two particles both with spin up or down and two particles with opposite spins.

(d) For a state with $m = 3$ particles,

$$\begin{aligned}\lambda^{(\pm)}_{\downarrow\uparrow\sigma} &= \boldsymbol{D}_3 + U + 2V \pm t,\\ |S^{(\pm)}_{\downarrow\uparrow\sigma}\rangle &= \frac{1}{\sqrt{2}}(|\downarrow\uparrow,\sigma\rangle \mp |\sigma,\downarrow\uparrow\rangle).\end{aligned} \qquad (14)$$

The states $|S^{(\pm)}_{\downarrow\uparrow\sigma}\rangle$ correspond to two particles with opposite spin and one spin.

(e) For a state with $m = 4$ particles,

$$\lambda_{\downarrow\uparrow\downarrow\uparrow} = \boldsymbol{D}_4 + 2U + 4V, \quad |S_{\downarrow\uparrow\downarrow\uparrow}\rangle = |\downarrow\uparrow,\downarrow\uparrow\rangle. \qquad (15)$$

The state $|S_{\downarrow\uparrow\downarrow\uparrow}\rangle$ means there are two spins at each site with opposite spins.

It is worth noting that the Hamiltonian (2) has 256 eigenvalues per diamond plaquette.

From hereon, to make our discussion more realistic, we will only consider the repulsive on-site Coulomb interaction ($U > 0$) and the repulsive Coulomb interaction between nearest neighbors ($V > 0$). Afterward, we will discuss the phase diagram at zero temperature.

The present model exhibits nine states, which are tabulated in Table I, for all possible numbers of particles available in the chain. For the empty particle and the fully filled particles, we have the states $|\mathsf{S_0}\rangle = |\mathsf{Vac}\rangle$ and $|\mathsf{S_6}\rangle = |\mathsf{Full}\rangle$, respectively. For one particle per unit cell and five particles per unit cell, we also have one corresponding frustrated state $|\mathsf{S_1}\rangle = |\mathsf{FRU_1}\rangle$ and the state $|\mathsf{S_5}\rangle = |\mathsf{FRU_5}\rangle$, respectively. However, for two particles per unit cell, we have two states. One configuration is an antiferromagnetic state ($|\mathsf{S_2}\rangle = |\mathsf{AFM_2}\rangle$), whereas the other configuration is a frustrated state ($|\bar{\mathsf{S}}_2\rangle = |\mathsf{FRU_2}\rangle$). Due to particle-hole symmetry, the analysis for the case of four particles (or two holes) becomes analogous for the case of two particles, hence we have one antiferromagnetically ordered state ($|\mathsf{S_4}\rangle = |\mathsf{AFM_4}\rangle$) and another frustrated state ($|\bar{\mathsf{S}}_4\rangle = |\mathsf{FRU_4}\rangle$). Furthermore, for the special case of half-filled particles (with three particles or holes per unit cell), we could also have two possible states: one frustrated state $|\mathsf{S_3}\rangle = |\mathsf{FRU_3}\rangle$ and another antiferromagnetically ordered state ($|\bar{\mathsf{S}}_3\rangle = |\mathsf{AFM_3}\rangle$). However, the case $|\mathsf{AFM_3}\rangle$ occurs only

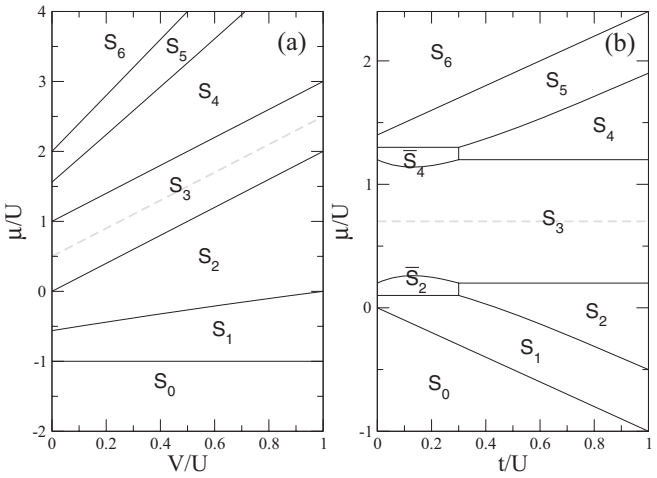

FIG. 2. Phase diagrams at zero temperature: (a) the phase diagram of V/U vs μ/U for a fixed value of $t/U = 1$; (b) the phase diagram of t/U vs μ/U for a fixed value of $V/U = 0.25$.

when $V > U$. We ignore this case since it is too artificial. In Fig. 2, we illustrate the phase transition of these states at zero temperature. In Fig. 2(a), we illustrate the phase diagram of V/U versus μ/U for a fixed value of $t/U = 1$, where we display seven states S_i ($i = 0, \ldots, 6$). In Fig. 2(b), we display the phase diagram of t/U versus μ/U for a fixed value of $V/U = 0.25$. This phase diagram illustrates nine states: the seven states already shown in Fig. 2(a) and two additional ones, $|\mathsf{FRU}_2\rangle$ and $|\mathsf{FRU}_4\rangle$. The full transition boundary functions between states are tabulated in Table II. The first and third columns correspond to the boundary states, while the second and fourth columns correspond to the boundary functions.

In Fig. 2, a dashed line represents the half-filled band curve of the extended Hubbard model on a diamond chain.

Other variants of the phase diagram at zero temperature could also be discussed, although the main properties have already been shown in Fig. 2.

TABLE II. The first and third columns represent the boundary between two states tabulated in Table I, while the second and fourth columns denote the function of the boundaries. For simplicity, we use the notation $V' = V/U$ and $t' = t/U$.

State	$V' \times \mu/U$ [Fig. 2(a)]	State	$t' \times \mu/U$ [Fig. 2(b)]
$\mathsf{S}_0, \mathsf{S}_1$	-1	$\mathsf{S}_0, \mathsf{S}_1$	$-t'$
$\mathsf{S}_1, \mathsf{S}_2$	$\frac{3+V'-\sqrt{(V'-1)^2+16}}{2}$	$\mathsf{S}_1, \mathsf{S}_2$	$\frac{11-10\sqrt{0.81+16t'^2}+20t'}{20}$
$\mathsf{S}_2, \mathsf{S}_3$	$2V'$	$\mathsf{S}_2, \mathsf{S}_3$	$\frac{1}{5}$
$\mathsf{S}_3, \mathsf{S}_4$	$2V'+1$	$\mathsf{S}_3, \mathsf{S}_4$	$\frac{6}{5}$
$\mathsf{S}_4, \mathsf{S}_5$	$\frac{-1+7V'-\sqrt{(V'-1)^2+16}}{2}$	$\mathsf{S}_4, \mathsf{S}_5$	$\frac{17-20t'+5\sqrt{0.81+16t'^2}}{20}$
$\mathsf{S}_5, \mathsf{S}_6$	$4V'+2$	$\mathsf{S}_5, \mathsf{S}_6$	$t'+\frac{7}{5}$
		$\mathsf{S}_5, \bar{\mathsf{S}}_4$	$\frac{13}{10}$
		$\bar{\mathsf{S}}_4, \mathsf{S}_3$	$\frac{-4t'+3+2\sqrt{0.81+16t'^2}}{4}$
		$\mathsf{S}_3, \bar{\mathsf{S}}_2$	$\frac{20t'+13-10\sqrt{0.81+16t'^2}}{20}$
		$\bar{\mathsf{S}}_2, \mathsf{S}_1$	$\frac{1}{10}$

IV. EXACT SOLUTION

The method we will use will be the decoration transformation proposed earlier by Syozi [43] and Fisher [44]. This approach was the subject of a later study by Rojas *et al.* [45] for the case of multispins, and by Strečka [46] for the hybrid system (e.g., Ising-Heisenberg). Another interesting variant of this approach is also discussed by us, where we propose a direct transformation instead of several step-by-step ones [47]. An illustrative successful application of this last approach was performed in Ref. [48]. The decoration transformation approach is widely used to solve spin models, however it can also be applied to the electron coupling system. This was done by the authors of Ref. [24] for the case of a spinless fermion on a diamond structure.

In order to use the decoration transformation approach, we write the Boltzmann factor for the extended Hubbard model on a diamond chain as follows:

$$\begin{aligned} w_{\boldsymbol{n}_i^c, \boldsymbol{n}_{i+1}^c} &= e^{-\beta \boldsymbol{D}_0} + 4(e^{-\beta \boldsymbol{D}_1} + e^{-\beta(\boldsymbol{D}_3+U+2V)})\cosh(\beta t) \\ &\quad + e^{-\beta \boldsymbol{D}_2}(e^{-\beta U} + 3e^{-\beta V}) + e^{-\beta(\boldsymbol{D}_4+2U+4V)} \\ &\quad + e^{-\beta(\boldsymbol{D}_2+V)}(e^{-\beta\theta_+ t/2} + e^{-\beta\theta_- t/2}), \end{aligned} \tag{16}$$

where the $\theta_\pm$ were already defined in Eq. (13).

The extended Hubbard model on a diamond chain can be mapped onto an effective extended Hubbard-like model in the atomic limit, where it involves additional three-body and four-body interactions. Therefore, the effective extended Hubbard model becomes

$$\begin{aligned} &\tilde{\boldsymbol{H}}_{i,i+1} \\ &= -\tilde{\mu}\boldsymbol{n}_i^c + \tilde{U}\boldsymbol{n}_{i,\uparrow}^c \boldsymbol{n}_{i,\downarrow}^c + \tilde{V}\left(\boldsymbol{n}_{i,\uparrow}^c + \boldsymbol{n}_{i,\downarrow}^c\right)\left(\boldsymbol{n}_{i+1,\uparrow}^c + \boldsymbol{n}_{i+1,\downarrow}^c\right) \\ &\quad + \tilde{W}_3 \boldsymbol{n}_{i,\uparrow}^c \boldsymbol{n}_{i,\downarrow}^c \left(\boldsymbol{n}_{i+1,\uparrow}^c + \boldsymbol{n}_{i+1,\downarrow}^c\right) + \tilde{W}_4 \boldsymbol{n}_{i,\uparrow}^c \boldsymbol{n}_{i,\downarrow}^c \boldsymbol{n}_{i+1,\uparrow}^c \boldsymbol{n}_{i+1,\downarrow}^c, \end{aligned} \tag{17}$$

where $\tilde{\mu}$ could be interpreted as an effective chemical potential. In a similar way, $\tilde{U}$ denotes the on-site Coulomb

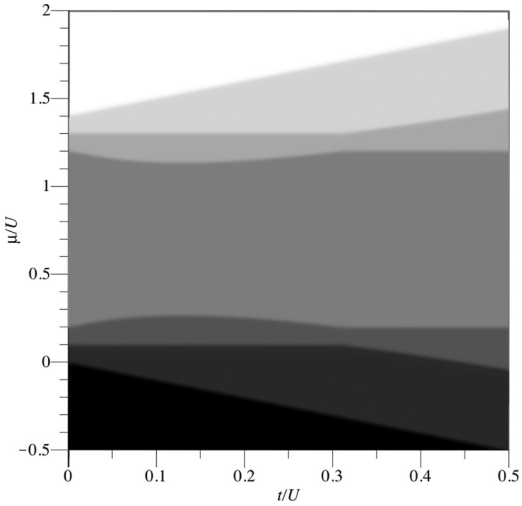

FIG. 3. Electronic density per site for $T/U = 0.01$ and $V/U = 0.1$ as a function of t/U and μ/U. The black region corresponds to empty particles while the white region corresponds to fully filled electrons or empty holes. Different levels of gray represent the intermediate electronic density.

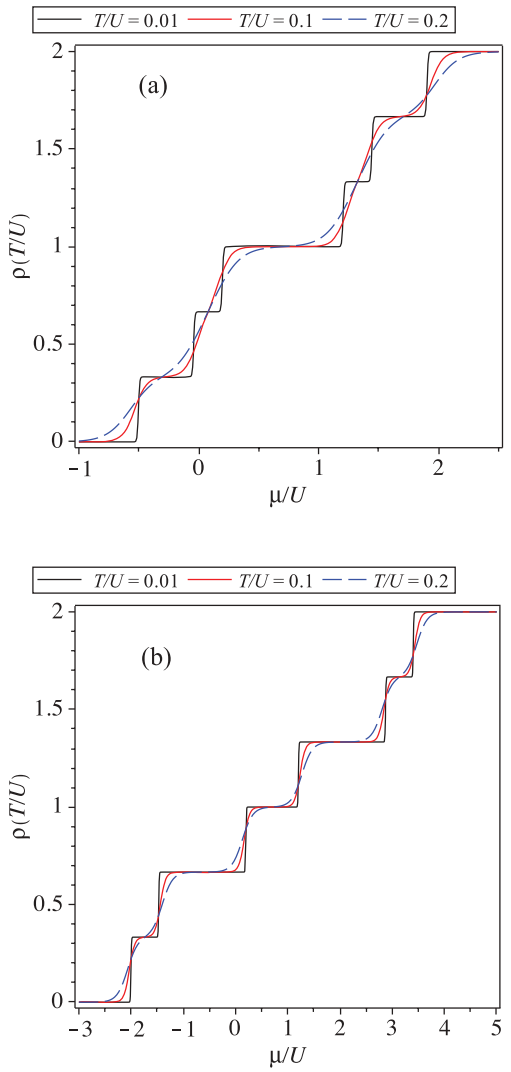

FIG. 4. (Color online) Electronic density as a function of chemical potential for a fixed value of $V/U = 0.1$. (a) $t/U = 0.5$ and (b) $t/U = 2.0$

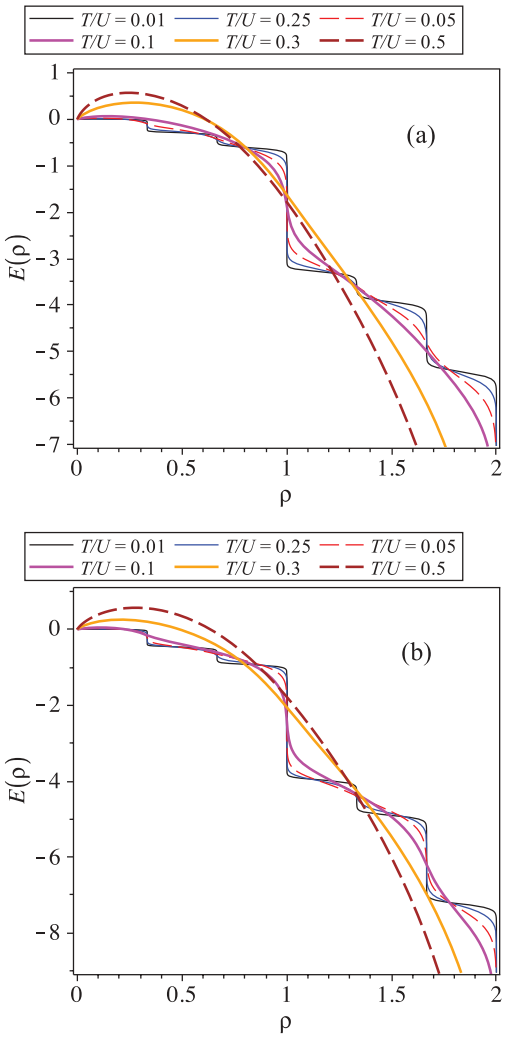

FIG. 5. (Color online) Internal energy $\mathscr{E}(\rho)$ as a function of electronic density ρ for a given value of $V/U = 0.1$. (a) $t/U = 0.2$ and (b) $t/U = 0.5$

repulsion coupling while $\tilde{V}$ corresponds to the nearest-neighbor repulsion coupling. The term $\tilde{W}_3$ will be interpreted as a three-body interaction term and W_4 will be a four-body coupling term. All of the above parameters could be obtained as a function of the Hamiltonian (2) parameters when the decoration transformation is performed

The Boltzmann factor for the effective Hubbard model in the atomic limit becomes

$$\tilde{w}_{\boldsymbol{n}_i^c,\boldsymbol{n}_{i+1}^c} = A\, e^{-\beta \tilde{\boldsymbol{H}}_{i,i+1}}, \tag{18}$$

where the factor A is an additional variable to be determined in terms of the original Hamiltonian (2). With use of the decoration transformation [43–45], we will impose the following condition:

$$w_{\boldsymbol{n}_i^c,\boldsymbol{n}_{i+1}^c} = \tilde{w}_{\boldsymbol{n}_i^c,\boldsymbol{n}_{i+1}^c}. \tag{19}$$

Using Eq. (19), we can find all the parameters of the effective Hamiltonian (17) and the factor A.

To solve the effective Hubbard model with up to four-body coupling, we can use the transfer-matrix method [49], which is similar to that used in Refs. [24,50]. Therefore, we symmetrize the Hamiltonian by exchanging $i \to i+1$ and $i+1 \to i$, thus the transfer matrix becomes symmetric. For our case, this transfer matrix can be expressed by

$$\mathbf{T} = \begin{bmatrix} w_{0,0} & w_{0,1} & w_{0,1} & w_{0,2} \\ w_{0,1} & w_{1,1} & w_{1,1} & w_{1,2} \\ w_{0,1} & w_{1,1} & w_{1,1} & w_{1,2} \\ w_{0,2} & w_{1,2} & w_{1,2} & w_{2,2} \end{bmatrix}, \tag{20}$$

where the Boltzmann factor is given by Eq. (16), and we use a convenient notation, such as

$$w_{0,0}(x) = 1 + 2x\left(1 + \frac{x^2}{z^4 y^2}\right)\left(\frac{1}{\gamma^2} + \gamma^2\right) + x^2\left(\frac{3}{z^2} + \frac{1}{y^2} + \frac{1}{yz\varsigma} + \frac{\varsigma}{yz}\right) + \frac{x^4}{y^4 z^8}, \tag{21}$$

with $x = e^{2\beta\mu}$, $y = e^{\frac{1}{2}\beta U}$, $z = e^{\frac{1}{2}\beta V}$, $\gamma = e^{\frac{1}{2}\beta t}$, and $\varsigma = e^{\frac{1}{2}\beta\sqrt{(U-V)^2+16t^2}}$. The remaining Boltzmann factors could be expressed easily through the function $w_{0,0}(x)$ defined in Eq. (21) as follows:

$$w_{n_1,n_2}(x) = \frac{x^{(n_1+n_2)/2}}{y^{[n_1/2]+[n_2/2]}} w_{0,0}\left(\frac{x}{z^{n_1+n_2}}\right), \tag{22}$$

where $[\cdots]$ indicates the lowest integer of any real number. Thereafter, all elements of matrix (20) are well expressed just in terms of $w_{0,0}(x)$.

The Boltzmann factors for the effective Hubbard model (18) with three- and four-body terms are given by

$$\begin{aligned}
\tilde{w}_{0,0} &= A, \\
\tilde{w}_{0,1} &= Ar, \quad r = e^{\beta\tilde{\mu}/2}, \\
\tilde{w}_{0,2} &= Ars, \quad s = e^{-\beta\tilde{U}/2}, \\
\tilde{w}_{1,1} &= Ar^2t, \quad t = e^{-\beta\tilde{V}}, \\
\tilde{w}_{1,2} &= Ar^3st^2u, \quad u = e^{-\beta\tilde{W}_3/2}, \\
\tilde{w}_{2,2} &= Ar^4s^2t^4u^4v.
\end{aligned} \tag{23}$$

The determinant of the transfer matrix becomes a quartic equation of the form $\det(\mathbf{T} - \Lambda) = \Lambda^4 + a_3\Lambda^3 + a_2\Lambda^2 + a_1\Lambda$, where the coefficients become

$$\begin{aligned}
a_1 &= -2w_{0,0}w_{1,1}w_{2,2} + 2w_{0,2}^2w_{1,1} + 2w_{0,1}^2w_{2,2} \\
&\quad + 2w_{0,0}w_{1,2}^2 - 4w_{0,2}w_{0,1}w_{1,2}, \\
a_2 &= -2w_{0,1}^2 + 2w_{0,0}w_{1,1} + w_{0,0}w_{2,2} \\
&\quad + 2w_{1,1}w_{2,2} - w_{0,2}^2 - 2w_{1,2}^2, \\
a_3 &= -w_{0,0} - w_{2,2} - 2w_{1,1},
\end{aligned} \tag{24}$$

The coefficients can also be expressed using the effective Hamiltonian parameters, thus the coefficients of the quartic equation are given by

$$\begin{aligned}
a_1 &= A(-2r^6t^5s^2u^4v + 2r^6s^2t + 2r^6s^2t^4u^4v \\
&\quad + 2r^6s^2t^4u^2 - 4r^6s^2t^2u), \\
a_2 &= A(-2r^2 + 2r^2t + r^4s^2t^4u^4v + 2r^6t^5s^2u^4v \\
&\quad - r^4s^2 - 2r^6s^2t^4u^2), \\
a_3 &= -A(1 + r^4s^2t^4u^4v + 2r^2t).
\end{aligned} \tag{25}$$

Therefore, the roots of the algebraic quartic equation may be reduced to a cubic equation, the solutions of which are given as follows:

$$\Lambda_j = 2\sqrt{Q}\cos\left(\frac{\phi + 2\pi j}{3}\right) - \frac{1}{3}a_3, \quad j = 0,1,2, \tag{26}$$

with

$$\begin{aligned}
\phi &= \arccos\left(\frac{R}{\sqrt{Q^3}}\right), \quad Q = \frac{a_3^2 - 3a_2}{9}, \\
R &= \frac{9a_2a_3 - 27a_1 - 2a_3^3}{54}.
\end{aligned} \tag{27}$$

Furthermore, we also have an additional trivial solution $\Lambda_3 = 0$ of the algebraic quartic equation.

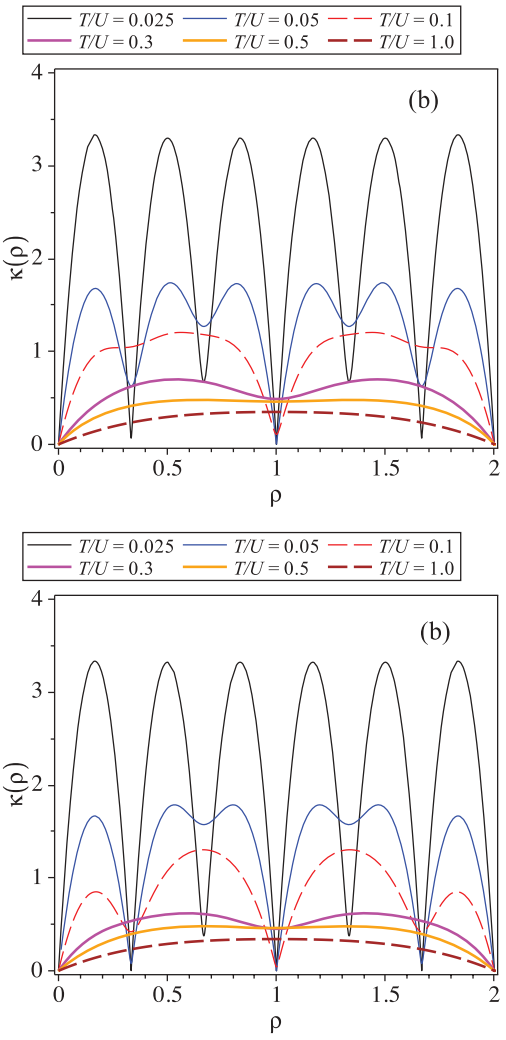

FIG. 6. (Color online) The compressibility $\kappa(\rho)$ as a function of electronic density ρ for a fixed value of $V/U = 0.1$. (a) $t/U = 0.2$ and (b) $t/U = 0.5$.

Hence, the largest eigenvalue of the transfer matrix will be Λ_0, which is expressed by Eq. (26). Once the largest eigenvalue of the transfer matrix is known, we are able to obtain the partition function straightforwardly, and thereafter the free energy is given by $f = -\frac{1}{\beta}\ln(\Lambda_0)$. Using the free energy per unit cell, we may obtain the thermodynamic properties and how the model behaves when the number particles are changing away from the half-filled band.

V. THERMODYNAMIC PROPERTIES

In order to study the thermodynamic properties, we will use the exact free energy $f = -\frac{1}{\beta}\ln(\Lambda_0)$ as a starting point. Therefore, we will proceed to discuss the thermodynamic properties as a function of temperature, chemical potential, and electronic density. To make our discussion more realistic, we will assume that we are considering only the repulsive on-site Coulomb interaction ($U > 0$) and the repulsive Coulomb interaction between nearest neighbors ($V > 0$).

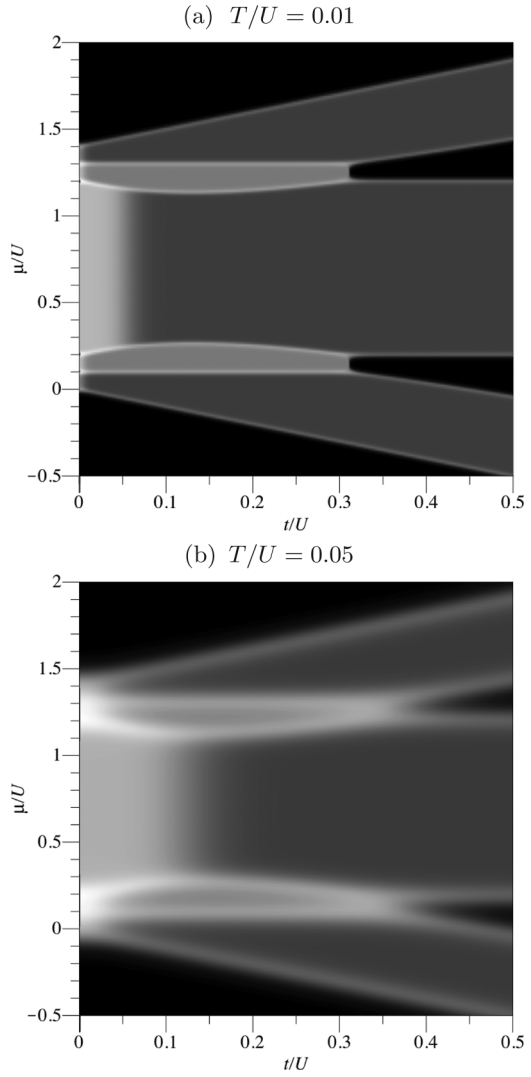

FIG. 7. Entropy as a function of t/U and μ/U for a fixed value of $U/V = 0.1$. The black region corresponds to nonfrustrated entropy while the white region corresponds to the higher residual entropy effect. Gray areas correspond to the intermediate residual entropy effect.

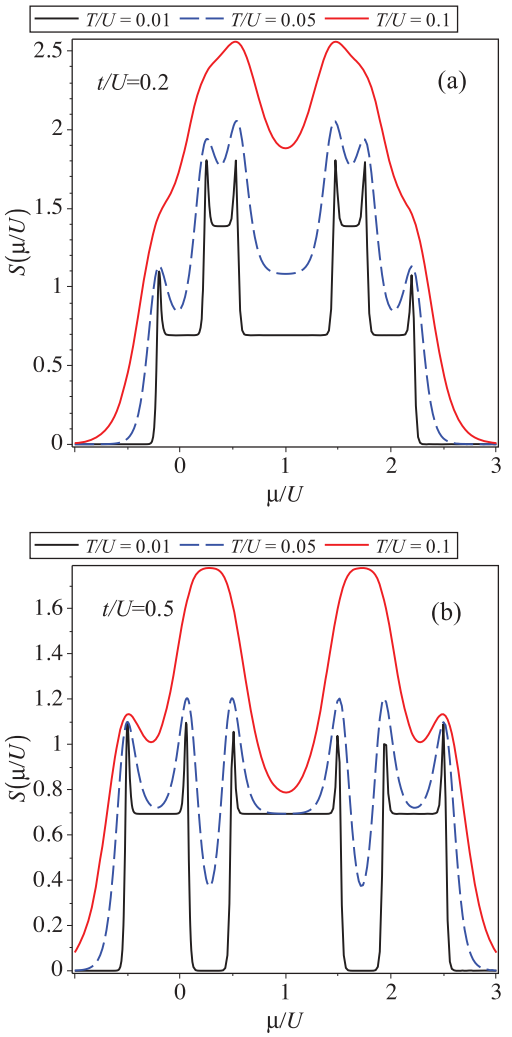

FIG. 8. (Color online) Entropy $\mathcal{S}$ against μ at low temperature assuming a fixed value of $V/U = 0.25$. (a) $t/U = 0.2$ and (b) $t/U = 0.5$.

A. The electronic density

We will explore the electronic density $\rho = -\frac{\partial f}{\partial \mu}$ as a function of chemical potential as well as the hopping term. In Fig. 3, we plot the chemical potential μ/U versus t/U for a fixed value of temperature $T/U = 0.01$ and nearest-neighbor coupling $V/U = 0.1$. Gray scale indicates electronic density between $0 < \rho < 2$. The darkest region corresponds to the lowest electronic density while the brightest region corresponds to fully filled electrons.

In Fig. 4(a), we plot the electronic density as a function of chemical potential at low temperature for a fixed value of the hopping term $t/U = 0.5$ and $V/U = 0.1$. Six plateaus are visible at $\rho = 0$, $1/3$, $2/3$, 1, $4/3$, $5/3$, and 2, and this phenomenon vanishes as soon as the temperature increases. In Fig. 4(b), we plot the same quantity but for a large hopping term $t/U = 2$ and $V/U = 0.1$. In this case, the plateaus correspond to electronic densities $\rho = 1/3, 2/3, 4/3$, and $5/3$, which turn away from the half-filled band $\rho = 1$. Moreover, the plateaus for densities $2/3$ and $4/3$ become larger, as we can see in Fig. 4, which is also in agreement with Fig. 3.

B. The internal energy

The internal energy $\mathscr{E} = -\frac{\partial \ln(\Lambda_0)}{\partial \beta}$ for the extended Hubbard model will be discussed as a function of electronic density. In Fig. 5(a), the internal energy is plotted for a small hopping term $t/U = 0.2$ and $V/U = 0.1$. This internal energy exhibits a gap energy (steplike function) at zero temperature when the electronic density changes, but when temperature increases the steplike function becomes smoother. In Fig. 5(b), the internal energy is plotted for a hopping term $t/U = 0.5$ and $V/U = 0.1$, and the shape of the curves is basically similar to that at $t/U = 0.2$. In summary, Fig. 5 displays the electronic density dependence as well as the temperature dependence. We can see that the larger the electronic density is, the lower the energy becomes, although for low density around $\rho = 0.5$ there is a maximum of internal energy. We also notice for several fixed

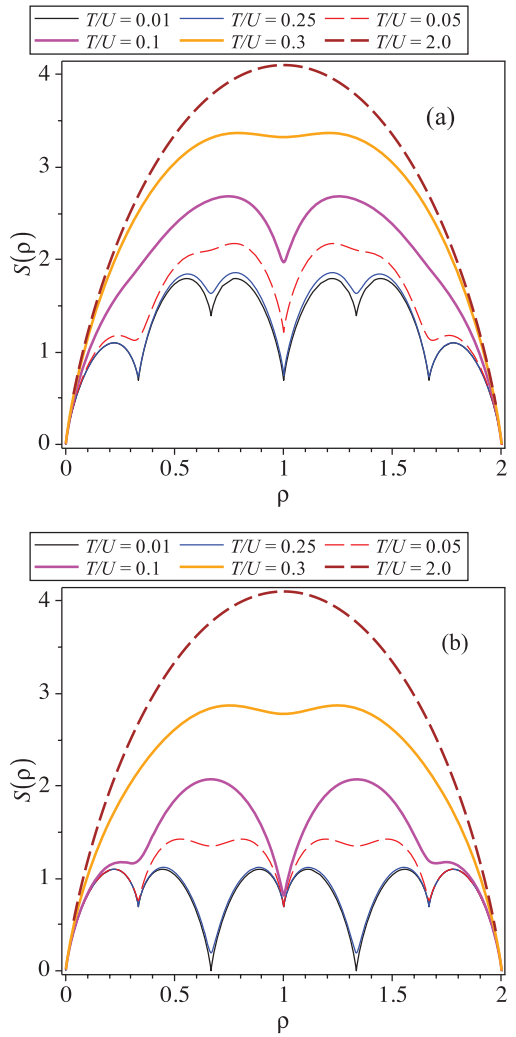

FIG. 9. (Color online) Entropy against electronic density assuming fixed Coulomb coupling $V/U = 0.1$. (a) $t/U = 0.2$ and (b) $t/U = 0.5$.

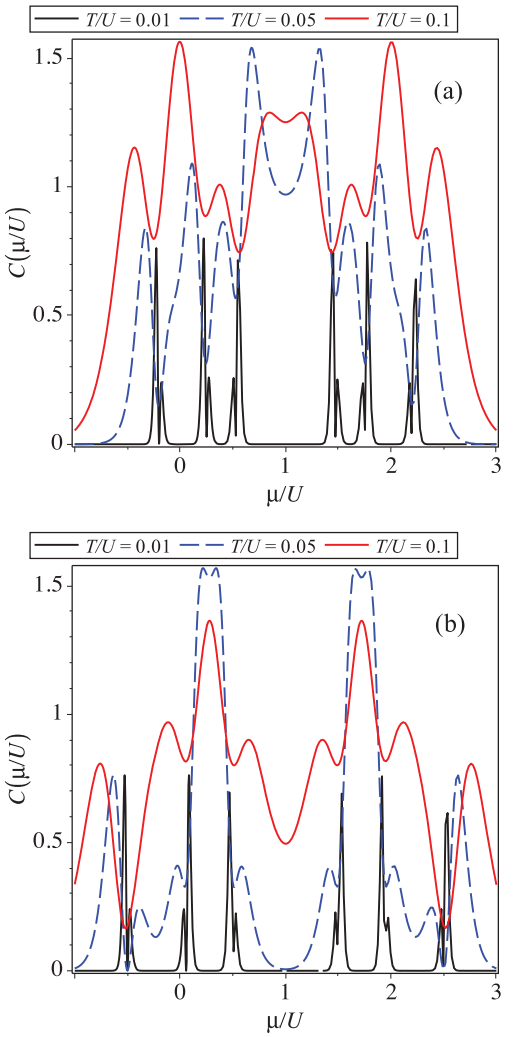

FIG. 10. (Color online) The specific heat vs the chemical potential for low temperature for a fixed value of $V/U = 0.25$. (a) $t/U = 0.2$ and (b) $t/U = 0.5$.

values of temperature that the plot for the internal energy becomes smooth for sufficiently high temperature.

C. Compressibility

Another interesting amount that we could discuss is the compressibility defined by $\kappa(\rho) \equiv \frac{\partial \rho}{\partial \mu}$. This value makes it more convenient to study electron particles, rather than the compressibility sometimes known as total compressibility [49], $\kappa_T = -\frac{1}{\rho^2}\frac{\partial^2 f}{\partial \mu^2} = \frac{\kappa}{\rho^2}$. Therefore, compressibility will be discussed as a function of Hamiltonian parameters, temperature, and electronic density. In Fig. 6, we display the compressibility behavior as a function of the electronic density on the diamond chain for a fixed value of $V/U = 0.1$. In Fig. 6(a), we fixed the hopping term at $t/U = 0.2$. This is roughly below the phase transition that occurs at $t/U = 0.3$, where we display how the compressibility behaves at low temperature. The compressibility becomes minimum (harder) close to the fractional electronic densities 0, 1/3, 2/3, 1, 4/3, 5/3, and 2. In contrast, there are six local maxima (softer) between fractional densities 1/3, 2/3, 1, 4/3, 5/3, and 2 for temperature lower than $T/U \lesssim 0.05$. For $0.05 \lesssim T/U \lesssim 0.5$, there is just one minimum at $\rho = 1$ in addition to the minima at $\rho = 0$ and 2. Furthermore, for higher temperature $T/U \gtrsim 0.5$, the compressibility exhibits just one maximum at electronic density $\rho = 1$. Figure 6(b) is illustrated for $t/U = 0.5$, roughly above the phase transition. In principle, the behavior is quite similar to that shown in Fig. 6(a), i.e., a low compressibility survives for higher temperature $t/U = 0.1$ at the half-filled band $\rho = 1$. However, when the temperature is sufficiently high ($0.3 \lesssim T/U \lesssim 0.5$), there is only one minimum at $\rho = 1$ in addition to empty (full) electrons (holes), whereas for $T/U \gtrsim 0.5$, just a simple maximum is shown at $\rho = 1$.

D. The entropy

We will study another interesting quantity, namely the entropy $\mathcal{S} = -\frac{\partial f}{\partial T}$, and how it behaves when the Hamiltonian parameters, the temperature, or even the electronic density change. In Fig. 7, we illustrate the magnitude of entropy

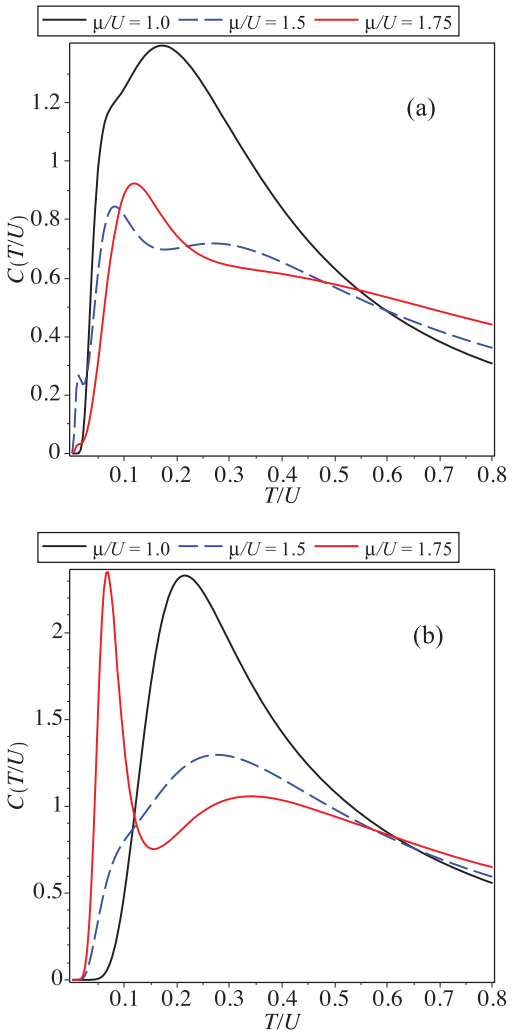

FIG. 11. (Color online) The specific heat vs temperature for a given value of $V/U = 0.25$ and different values of chemical potential. (a) $t/U = 0.2$ and (b) $t/U = 0.5$.

as a function of t/U and μ/U, assuming a fixed value of $V/U = 0.1$. Different levels of gray scale represent the magnitude of entropy; the darkest region corresponds to the lowest entropy while the brightest region corresponds to higher entropy. At low temperature, the large value of entropy is related to the influence of the residual entropy. When the temperature increases, the entropy curves become softer, as displayed in Fig. 7(a) for $T/U = 0.01$ and in Fig. 7(b) for $T/U = 0.05$.

In Fig. 8, we display the entropy $\mathcal{S}(\mu)$ as a function of chemical potential, assuming a fixed value of $V/U = 0.25$, where we are able to illustrate the residual entropy effect in agreement with Fig. 7. The entropy indicates several peaks via the chemical potential. Figure 8(a) is plotted for $t/U = 0.2$, where the influence of two types of residual entropy is shown around of $\mathcal{S} = \ln(2)$ and $\ln(3)$. Figure 8(b) is plotted for $t/U = 0.5$. In this case, we only display the influence of the residual entropy of $\mathcal{S} = \ln(2)$. It is clear that as the temperature increases we have an increase of entropy as well, however for large $|\mu|$ the entropy is smaller than for small $\mu \approx 1$.

In Fig. 9, we display the entropy as a function of electronic density assuming a given parameter $V/U = 0.1$ for a fixed value of parameter $V/U = 0.1$. For high temperature $T \geqslant 2$, the entropy reaches its highest point at $\rho = 1$. We can see that the residual entropy is strongly related to the electronic density. We also indicate that there is no residual entropy for a fully electronic density, therefore the entropy becomes lower even for high temperature.

For electronic density $\rho = 1/3$ and $2/3$, the residual entropy is $\mathcal{S} = \ln(2)$, while for $\rho = 4/3$ and $5/3$, larger residual entropy is displayed, $\mathcal{S} = \ln(4)$.

E. The specific heat

Finally, we will discuss the behavior of the specific heat, $C = -T\frac{\partial^2 f}{\partial T^2}$, for the extended Hubbard model in the quasi-atomic limit. Thus, let us start by displaying the specific heat as a function of chemical potential, which is illustrated in Fig. 10 for a fixed value of $V/U = 0.25$. In the low-temperature limit, we can see the effect of the phase transition at zero temperature with very sharp peaks when the temperature decreases. In particular, in Fig. 10(a) we display the specific heat as a function of μ/U for $t/U = 0.2$, while in Fig. 10(b) we show the specific heat as a function of μ/U for $t/U = 0.5$.

Lastly, in Fig. 11 we display the specific heat as a function of temperature assuming the nearest-neighbor Coulomb interaction $V/U = 0.25$. Figure 11(a) is plotted for $t/U = 0.2$, while in Fig. 11(b) we assume $t/U = 0.5$. We can see very sharp peaks as the temperature decreases. These anomalous peaks appear due to low-lying energy around the first-order phase transition at zero temperature.

VI. CONCLUSIONS

The proposed Hubbard model on a diamond chain was discussed at zero temperature as well as at finite temperature. The phase diagram at zero temperature displays four frustrated states and five nonfrustrated states that are ordered antiferromagnetically. With regard to finite-temperature properties, this model can be solved exactly through decoration transformation [43–45,47]. The transfer-matrix technique [49] enables us to map the proposed model onto an exact Hubbard model in the atomic limit with three- and four-body couplings. Therefore, detailed thermodynamic properties were discussed, including the density as a function of chemical potential, illustrating six plateaus. Internal energy was also considered as a function of electronic density far away from the half-filled band for several fixed temperatures. We also studied compressibility. Once again, we illustrated this amount as a function of electronic density, and so we can conclude that the diamond chain is more compressible at low temperature when the electronic density is between 1/3, 2/3, 1, 4/3, and 5/3, respectively. As soon as the temperature increases, the compressibility decreases, becoming a simple decreasing curve as a function of density. We also considered the entropy as another interesting amount. This amount was studied as a function of chemical potential as well as electronic density, where we clearly observed the residual entropy contribution due to geometrical frustration. Finally, we discussed the specific heat as a function

of chemical potential and temperature. In the near future, we plan to study the Coulomb interaction between the nodal (monomer-monomer) sites and a different type of interaction between the nodal-interstitial (dimer-monomer) sites, both positive and negative, at the quantum level. This explains the wide range of experiments on the diamond chain.

ACKNOWLEDGMENTS

O.R. and S.M.d.S. thank CNPq and Fapemig for partial financial support. This work has been supported by the French-Armenian Grant No. CNRS IE-017 (N.A.) and by the Brazilian FAPEMIG Grant CEX - BPV - 00028-11 (N.A.).

[1] E. H. Lieb, *Condensed Matter Physics and Exactly Soluble Models*, Selecta of E. H. Lieb, edited by B. Nachtergaele, J. P. Solovej, and J. Yngvason (Springer, Berlin, 2004).
[2] I. S. Hagemann, Q. Huang, X. P. A. Gao, A. P. Ramirez, and R. J. Cava, Phys. Rev. Lett. **86**, 894 (2001).
[3] J. van Lierop and D. H. Ryan, Phys. Rev. Lett. **86**, 4390 (2001).
[4] S. Eggert, Phys. Rev. B **54**, R9612 (1996).
[5] K. Okamoto and K. Nomura, Phys. Lett. A **169**, 433 (1992).
[6] N. Laflorencie and D. Poilblanc, Phys. Rev. Lett. **90**, 157202 (2003).
[7] S. Daul and R. M. Noack, Phys. Rev. B **61**, 1646 (2000).
[8] K. Hida, J. Phys. Soc. Jpn. **63**, 2359 (1994).
[9] V. R. Ohanyan and N. S. Ananikian, Phys. Lett. A **307**, 76 (2003).
[10] V. V. Hovhannisyan and N. S. Ananikian, Phys. Lett. A **372**, 3363 (2008).
[11] N. Ananikian, L. Ananikyan, R. Artuso, and H. Lazaryan, Phys. Lett. A **374**, 4084 (2010).
[12] A. N. Kocharian, G. W. Fernando, K. Palandage, and J. W. Davenport, Phys. Rev. B **74**, 024511 (2006).
[13] A. N. Kocharian, G. W. Fernando, K. Palandage, T. Wang, and J. W. Davenport, Phys. Lett. A **364**, 57 (2007).
[14] O. Derzhko, A. Honecker, and J. Richter, Phys. Rev. B **79**, 054403 (2009).
[15] O. Derzhko, J. Richter, A. Honecker, M. Maksymenko, and R. Moessner, Phys. Rev. B **81**, 014421 (2010).
[16] R. R. Montenegro-Filho and M. D. Coutinho-Filho, Phys. Rev. B **74**, 125117 (2006).
[17] F. Mancini, Eur. Phys. J. B **47**, 527 (2005).
[18] F. Mancini and F. P. Mancini, Phys. Rev. E **77**, 061120 (2008).
[19] J. Vidal, R. Mosseri, and B. Doucot, Phys. Rev. Lett. **81**, 5888 (1998); J. Vidal *et al.*, *ibid.* **85**, 3906 (2000); B. Doucot and J. Vidal, *ibid.* **88**, 227005 (2002).
[20] J. Rössler and D. Mainemer, Condens. Matter Phys. **13**, 13704 (2010).
[21] W. Z. Wang, Phys. Rev. B **72**, 125116 (2005).
[22] Z. Gulácsi, A. Kampf, and D. Vollhardt, Phys. Rev. Lett. **99**, 026404 (2007).
[23] Z. Gulácsi, A. Kampf, and D. Vollhardt, Prog. Theor. Phys. Suppl. **176**, 1 (2008).
[24] O. Rojas and S. M. de Souza, Phys. Lett. A **375**, 1295 (2011).
[25] A. A. Lopes and R. G. Dias, Phys. Rev. B **84**, 085124 (2011).
[26] A. Honecker, S. Hu, R. Peters J., and Ritcher, J. Phys.: Condens. Matter **23**, 164211 (2011).
[27] M. S. S. Pereira, F. A. B. F. de Moura, and M. L. Lyra, Phys. Rev. B **77**, 024402 (2008).
[28] M. S. S. Pereira, F. A. B. F. de Moura, and M. L. Lyra, Phys. Rev. B **79**, 054427 (2009).
[29] B. M. Lisnii, Low Temp. Phys. **37**, 296 (2011).
[30] J. Strečka, A. Tanaka, L. Čanova, and T. Verkholyak, Phys. Rev. B **80**, 174410 (2009).
[31] J. Strečka, A. Tanaka, and M. Jasčur, J. Phys.: Conf. Ser. **200**, 022059 (2010).
[32] L. Canova, J. Strecka, and M. Jascur, J. Phys.: Condens. Matter **18**, 4967 (2006).
[33] O. Rojas, S. M. de Souza, V. Ohanyan, and M. Khurshudyan, Phys. Rev. B **83**, 094430 (2011).
[34] J. S. Valverde, O. Rojas, and S. M. de Souza, J. Phys.: Condens. Matter **20**, 345208 (2008).
[35] B. M. Lisnii, Ukr. J. Phys. **56**, 1237 (2011).
[36] N. S. Ananikian, L. N. Ananikyan, L. A. Chakhmakhchyan, and O. Rojas, arXiv:1110.6406.
[37] K. C. Rule, A. U. B. Wolter, S. Sullow, D. A. Tennant, A. Bruhl, S. Kohler, B. Wolf, M. Lang, and J. Schreuer, Phys. Rev. Lett. **100**, 117202 (2008).
[38] H. Kikuchi, Y. Fujii, M. Chiba, S. Mitsudo, T. Idehara, T. Tonegawa, K. Okamoto, T. Sakai, T. Kuwai, and H. Ohta, Phys. Rev. Lett. **94**, 227201 (2005); H. Kikuchi *et al.*, Prog. Theor. Phys. Suppl. **159**, 1 (2005).
[39] A. Honecker and A. Lauchli, Phys. Rev. B **63**, 174407 (2001); H. Jeschke *et al.*, Phys. Rev. Lett. **106**, 217201 (2011); J. Kang *et al.*, J. Phys.: Condens. Matter **21**, 392201 (2009); K. Takano, K. Kubo, and H. Sakamoto, *ibid.* **8**, 6405 (1996); **15**, 5979 (2003).
[40] L. Chakhmakhchyan, N. Ananikian, L. Ananikyan, and C. Burdik, J. Phys.: Conf. Series **343**, 012022 (2012).
[41] Sh.-S. Deng, Sh.-J. Gu, and H.-Q. Lin, Phys. Rev. B **74**, 045103 (2006).
[42] B. Gu and G. Su, Phys. Rev. B **75**, 174437 (2007); Kang *et al.*, J. Phys.: Condens. Matter **21**, 392201 (2009); O. Derzhko and J. Richter, Eur. Phys. J. B **52**, 23 (2006); B. Gu and G. Su, Phys. Rev. Lett. **97**, 089701 (2006); H. Kikuchi, Y. Fujii, M. Chiba, S. Mitsudo, T. Idehara, T. Tonegawa, K. Okamoto, T. Sakai, T. Kuwai, and H. Ohta, *ibid.* **97**, 089702 (2006).
[43] I. Syozi, Prog. Theor. Phys. **6**, 341 (1951).
[44] M. Fisher, Phys. Rev. **113**, 969 (1959).
[45] O. Rojas, J. S. Valverde, and S. M. de Souza, Physica A **388**, 1419 (2009).
[46] J. Strečka, Phys. Lett. A **374**, 3718 (2010).
[47] O. Rojas and S. M. de Souza, J. Phys. A **44**, 245001 (2011).
[48] M. Rojas, O. Rojas, and S. M. de Souza, arXiv:1105.5130.
[49] R. J. Baxter, *Exactly Solved Models in Statistical Mechanics* (Academic, New York, 1982).
[50] G. Beni and P. Pincus, Phys. Rev. B **9**, 2963 (1974).